Dipolar and charged localized excitons in carbon nanotubes

Jan T. Glückert, Lyudmyla Adamska, Wolfgang Schinner, Matthias S. Hofmann, Stephen K. Doorn, Sergei Tretiak, and Alexander Högele

Phys. Rev. B **98**, 195413 — Published 12 November 2018

DOI: 10.1103/PhysRevB.98.195413

Electric field control of dipolar and charged localized excitons in carbon nanotubes

Jan T. Glückert[1], Lyudmyla Adamska[2], Wolfgang Schinner[1], Matthias S. Hofmann[1], Stephen K. Doorn[3], Sergei Tretiak[2], and Alexander Högele[1]

[1]*Fakultät für Physik, Munich Quantum Center, and Center for NanoScience (CeNS), Ludwig-Maximilians-Universität München, Geschwister-Scholl-Platz 1, D-80539 München, Germany*

[2]*Theory Division, Los Alamos National Laboratory, Los Alamos, New Mexico 87545, U.S.A. and*

[3]*Center for Integrated Nanotechnologies, Materials Physics and Applications Division, Los Alamos National Laboratory, Los Alamos, New Mexico 87545, U.S.A.*

Abstract

We study both experimentally and theoretically the fundamental interplay of exciton localization and polarization in semiconducting single-walled carbon nanotubes. From Stark spectroscopy of individual carbon nanotubes at cryogenic temperatures we identify localized excitons as permanent electric dipoles with dipole moments of up to 1 eÅ. Moreover, we demonstrate field-effect doping of localized excitons with an additional charge which results in defect-localized trions. Our findings, in qualitative agreement with theoretical calculations, not only provide fundamental insight into the microscopic nature of localized excitons in carbon nanotubes, they also signify their potential for sensing applications and may serve as guidelines for molecular engineering of exciton-localizing quantum dots in other atomically thin semiconductors including transition metal dichalcogenides.

Optical transitions of semiconducting carbon nanotubes (CNTs) are dominated by excitons[1,2] which exhibit strong antibunching in the photoluminescence (PL) in their localized limit[3]. Exciton localization can arise at unintentional defects with shallow potentials[4,5] or incidental proximal charges[6] and ensure non-classical emission statistics up to room-temperature[7] for excitons bound to deep traps of oxygen side-wall dopants[8,9]. Along with oxygen functionalization[8–10], covalent side-wall chemistry with aryl and alkyl functionality[11,12] provides a versatile molecular means to engineer the photophysics of semiconducting CNTs. Introduced in a moderate concentration, the decoration of CNT side-walls with covalent defects results in substantial modifications such as brightening of nanotube emission and increased quantum yields[8,11,13], axially pinned PL[14] and inhibited diffusion[15–17].

Defect-localized excitons in CNTs represent a viable resource for applications in quantum sensing and quantum cryptography. For the latter technology, CNTs may facilitate the development of robust single-photon sources with room-temperature operation in the telecom band by utilizing discrete optical transitions of defect-localized excitons[7,18]. Covalent chemistry is readily available to fine-tune the exciton PL energy[8–12], and recent successful integration of CNTs into optical cavities[19,20] has demonstrated Purcell enhancement and directional coupling of single-photon emission as means to increase the single-photon emission efficiency. Moreover, photoemission from trions can be obtained upon chemical doping[21–24] and potentially utilized to interface photons with the CNT spin degree of freedom[25] via schemes of spin-tagged optical transitions analogous to charged semiconductor quantum dots and nitrogen vacancy (NV) centers in diamond[26]. This spin-photon interface in turn should enable all-optical sensing of magnetic fields in analogy to magnetometry based on charged NV color centers[27,28]. Corresponding all-optical electrometry via the electric dipole moment of localized excitons[29–31] has demonstrated recently sensitivity to elementary charge fluctuations in the nanotube environment[32].

Our work identifies both essential elements - dipolar localized excitons and voltage-controlled trions - for the development of sensing devices based on carbon nanotubes. By embedding CNTs in a field-effect (FET) device, we performed Stark spectroscopy of localized nanotube excitons in a transverse electric field at cryogenic temperatures. Our experiments demonstrate that exciton localization is accompanied by static exciton polarization with an average localization-induced electric dipole moment of $\sim 0.3\ e$Å. The experimental findings agree qualitatively with ab-initio model calculations for excitons bound by oxygen defects

on the side-wall of a $(6,5)$ nanotube. Moreover, we found that defect potential traps can bind an additional charge to promote PL from defect-localized trions[23,33], with control over the charging state provided by the gate voltage.

To subject nanotubes to a transverse electric field we fabricated FET devices based on a metal-oxide-semiconductor sequence as illustrated in Fig. 1a. The FET devices were fabricated starting with a p^+-doped silicon back gate terminated by an insulating layer of $d_1 = 100$ nm thermal SiO_2 that was cleaned with standard solvents and subsequently exposed to an oxygen plasma before spin-coating micelle-encapsulated CoMoCat CNTs with a spatial density below $1\mu m^{-2}$. The CNT layer was subsequently covered by sputter deposition with an insulating layer of Al_2O_3 of variable thickness d_2 (with $d_2 = 7$, 17, 39 and 42 nm in four different sample layouts), and a semitransparent NiCr layer of 5 nm thickness. A gate voltage V_g applied between the top and the ground electrode resulted in a homogeneous transverse electric field F through $F = V_g/d$, with d being the total thickness of the oxide layers. The functionality of our FET devices with break-down voltages of ± 80 V at low temperatures, corresponding to transverse electric field strengths of up to ± 1 V/nm, was confirmed with capacitance-voltage spectroscopy.

Individual CNTs embedded in a FET device were studied with photoluminescence (PL) spectroscopy in a home-built confocal microscope at the temperature of liquid helium of 4.2 K. A Ti:sapphire laser tuned in the range of $730 - 900$ nm was used to excite the PL via phonon sidebands in continuous wave mode. The PL of individual CNTs was dispersed with a monochromator and recorded with a low-noise nitrogen-cooled silicon CCD. Our experiments focused on $(6,4)$ and $(9,1)$ chiral nanotubes with emission in the spectral range of $1.35 - 1.43$ eV[34]. Characteristic PL signatures of individual nanotubes in our device are shown in Fig. 1b and c. Most of the CNTs were found to exhibit either a single-peak PL emission with an asymmetric lineshape (labelled as X in Fig. 1b) characteristic of disorder-localized excitons[35,36] or a two-peak emission spectrum (denoted as X and X^* in Fig. 1c). In our experiments, we assign one-peak spectra to excitons localized by environmental disorder, and two-peak spectra to exciton PL from oxygen-dopant sites introduced on CNT side-walls by sputter deposition of Al_2O_3[10].

The evolution of the CNT spectra with a single-peak and a double-peak spectrum as a function of the transverse electric field are shown in Fig. 2b and c, respectively. The electric field strength and orientation was varied proportional to the zig-zag voltage ramp shown

in Fig. 2a. The gate voltage was changed in discrete steps between maximum positive and negative values, with V_{max} ranging between 15 V and 30 V depending on the device. After each voltage step a PL spectrum was acquired for an incremental build-up of PL intensity false-color plots as in Fig. 2b for a single-peak emission, and in Fig. 2c for the X and X^* peaks. We repeated this procedure on more than 50 individual CNTs. Roughly one third of the tubes we have investigated showed irregular responses such as non-monotonic energy jumps or irreversible intensity fluctuations and were discarded from further analysis. The more regular responses as in Fig. 2b and c are representative for CNT excitons localized by incidental and oxygen-specific defect traps, respectively.

The vast majority of the nanotubes in our devices exhibited linear energy dispersions in response to the transverse electric field ramp, and both blue- and red-shifts were observed for different peaks (Fig. 2b and c). The linear slope, associated with the first-order Stark response of a permanent dipole, is in striking contrast to the second-order Stark effect expected for pristine CNTs. From a fitting procedure of CNT PL with single- and double-peak emission spectra as a function of the electric field strength according to $E(F) = E_0 - pF$ (red solid lines in Fig. 2b and c) we extracted the transverse dipole moment p of localized excitons with emission energy E_0 at $V_g = 0$ V. For the CNT in Fig. 2b, we obtained $p_X = -0.38\ e$Å, and for the two states X and X^* of Fig. 2c we determined $p_X = 0.36\ e$Å and $p_{X^*} = -0.26\ e$Å from linear fits to the data.

The results of the fitting procedure for all other CNTs with single- and double-peak emission are summarized in the histogram of Fig. 2d. It shows the distribution of the absolute value of the transverse permanent dipole moments determined for different CNTs and devices. The maximum value of the distribution at $|p| \simeq 0.7\ e$Å corresponds to an electron-hole separation of $\sim 10\%$ of the CNT diameter, a remarkably large value for a permanent dipole moment that is absent in pristine CNTs according to symmetry considerations. Another remarkable trend in our data are the anti-correlated signs of the dipole moments associated with X and X^* peaks (data points within the grey-shaded quadrants in Fig. 2e). Among the tubes with two-peak spectra, the majority exhibited positive p_X and negative p_{X^*} permanent dipole values (corresponding to data points in the lower right quadrant).

Our experimental observations suggest an intimate interplay of exciton localization and polarization which we confirmed by atomistic calculations of a $(6, 5)$ model nanotube in transverse electric field. The computations were performed using Gaussian09 software suite[37]

with B3LYP functional[38] and STO-3G basis set on 8-nm long segments of (6,5) carbon nanotube with hydrogen-terminated ends. In our calculations, the nanotube was embedded in a homogeneous medium with permittivity $\varepsilon_r = 6.3$ to account for the effective dielectric environment composed of Al_2O_3 ($\varepsilon_r = 9.3$) and Si_2O_2 ($\varepsilon_r = 3.9$) layers at the top and bottom of the tube and micellar encapsulation. The solvent effects were simulated in the framework of continuum polarizable conductor-like medium[39,40]. The geometry of both pristine and oxygen-doped CNTs was optimized in the presence of solvent at zero electric field, and the optical transition energies were calculated using Time-Dependent Density Functional Theory (TD-DFT).

Electric field was applied in transverse direction and optical transition energies were computed without additional geometry optimization. First, we modelled the response of a pristine tube and found a quadratic energy dispersion of the bright luminescent state with transverse polarizability $\alpha_\perp \simeq 7.7$ Å^2 in accord with previous estimates both from tight-binding[41–43] and first-principles calculations[44–46]. In stark contrast, for both bright peaks associated with an oxygen side-wall defect in ether-d configuration[9], our calculations yield predominantly linear dispersions (Fig. 3) when subjected to a transverse electric field of up to 0.2 V/nm.

The slopes and signs depend on the position of the defect on the nanotube side-wall as indicated by inset schematics in Fig. 3. Our calculations predict red- and blue-shifts for the X and X^* emission, respectively, with corresponding maximum values for the permanent dipole moments of 0.035 eÅ and -0.058 eÅ for a defect placed at the apex of the tube (left panel of Fig. 3). This defect geometry is expected to dominate our experiments with side-wall dopants introduced preferentially from the top by oxide sputtering, whereas localizing sites at the nanotube base caused by proximal charges[6] at the SiO_2 surface should be less frequent. Consistently, our experimental data of Fig. 2e reflects both the anti-correlated signs of the two-peak dispersions predicted by theory, and the different likelihood for defects to occur at the top and the bottom of the tubes (in the latter case the respective slopes would remain anti-correlated but interchange their signs). Experimental observation of dispersions as in the right panel of Fig. 3 should be rare because of the peripheral configuration of the related defects in the top-down sputter deposition process.

Both experiment and theory suggest that the radial symmetry of the electron-hole charge distribution is imbalanced at the exciton-localizing defect sites by field gradients associated

with defect traps, and both the strength and the orientation of the respective dipole moment depend on the specifics of the localizing defect. We note that the emergence of non-zero static exciton dipole moments from symmetry breaking is not limited to CNTs. Similar considerations explain finite transverse exciton dipole moments in two-dimensional semiconductors exhibiting different top and bottom dielectric environments[47–49] in contrast to theoretical calculations for ideal transition metal dichalcogenide monolayers[50,51] and experimental observation of a purely quadratic Stark effect in monolayers embedded between identical top and bottom dielectric substrates[52].

In our CNTs, localizing defect potentials should also act as traps for individual charges[14,23] and, in the presence of photoexcited electron-hole pairs, give rise to emission from energetically lower-lying trions[21–24,33,53]. Indeed, we observed signatures of such red-shifted PL satellites for some nanotubes within limited gate voltage ranges of our devices. Fig. 4a shows the PL response of a CNT to the gate voltage ramp as in Fig. 2a. The PL intensity is represented on a logarithmic false-color scale to enhance the visibility of the weak lowest-energy satellite which we assign to defect-localized trion PL emission (denoted in Fig. 4a as T; the sharp horizontal features unaffected by the gate voltage correspond to Raman scattered laser photons).

For the specific nanotube in Fig. 4, the T peak was observed around 1.24 eV in addition to X and X^* emission only at negative gate voltages. Other CNTs exhibited similar features only for positive voltages indicating that the polarity of the defect excess charge trapped out of the optically excited charge reservoir[53] depends on the defect potential details. Akin to previous experiments[21–24,33,53], the trion emission emerges at the expense of the main peak PL intensity (compare the relative intensities of T and X peaks at 0 V and -10 V in Fig. 4b). We note that the trion PL is weak because of experimental limitations in our setup. First, the use of a single aspheric lens instead of an apochromatic low-temperature objective resulted in different collection efficiencies for the PL of X and T peaks around 900 and 1000 nm, respectively. The second limiting factor was the spectral proximity of the trion emission wavelength to the detection cut-off of our silicon CCD. We estimate the reduction of the T peak intensity by $30-40$ times due to the combined effect of both experimental factors.

Further confirmation for the assignment of the voltage-induced satellite to trion emission comes from the inspection of the trion binding energy. We extract the energy scale associated

with the binding of an excess charge to the lowest defect-localized state by taking the energy splitting Δ_{TX^*} between the T and X^* emission peaks. This splitting, shown for all CNTs with charging signatures in the inset histogram of Fig. 4b, varies between 20 and 60 meV for the $(6,4)$ and $(9,1)$ narrow-diameter tubes in the spectral region of our experiment.

This trion binding energy is not to be confused with earlier experiments measuring the splitting between the trion peak and the E_{11} emission energy with excess contribution from exchange interactions[21,22,53,54]. It should be rather compared with the theoretical estimate of the bare trion binding energy[55], or with the energy splitting observed between the neutral and charged defect-localized emission peaks in diazonium-functionalized CNTs[23]. Theory predicts a trion binding energy of about 30 meV for a $(6,5)$ nanotube in a dielectric medium with $\varepsilon_r = 6$ (Ref.[55]). In aqueous suspension with $\varepsilon_r \simeq 2$, the corresponding experimental value of ~ 100 meV[23] was found in accord with the scaling of the trion binding energy with the dielectric constant as $\varepsilon_r^{-1.56}$ (Ref.[55]). Given the relatively high effective dielectric constant of the CNT environment in our FET devices and same diameters of $(6,5)$ and $(9,1)$ CNTs, we find very good agreement between our lower values of Δ_{TX^*} and theory. Consistently, the larger values in the distribution of Fig. 4b are associated with $(6,4)$ oxygen-doped nanotubes because of the inverse dependence of the trion binding energy on the tube diameter[55].

Our observation of defect-localized emission in combination with voltage-controlled charging places CNTs alongside semiconductor quantum dots[56] and NV centers[57] with charge-tunable emission characteristics and spin-projective optical transitions[26]. An intriguing advantage of CNTs for spin-based applications is expected to arise from prolonged electron spin coherence time in an isotopically engineered nuclear-spin free lattice[58]. Moreover, the absence of dangling bonds in sp^2-hybridized CNTs could enable long spin coherence times of electrons localized at engineered nanotube side-wall defects with immediate environmental proximity - a key factor for nanoscale-magnetometry[59,60] where near-surface color centers in diamond currently encounter major limitations due to unsaturated sp^3-bonds of the diamond crystal surface[61]. Finally, our results could inspire efforts to create chemically engineered quantum dots for in-plane confinement of excitons in emergent two-dimensional transition metal dichalcogenide semiconductors[62].

We thank J. P. Kotthaus, S. Rotkin, I. Bondarev and V. Perebeinos for useful discussions, P. Altpeter and R. Rath for assistance in the clean room, and P. Stallhofer from Wacker AG for providing the wafer material. This work was performed in part at the Center for Inte-

grated Nanotechnologies, a U.S. Department of Energy, Office of Science user facility. The research was funded by the European Research Council (ERC) under the grant agreement No. 336749 and the Deutsche Forschungsgemeinschaft (DFG) Cluster of Excellence NIM (Nanosystems Initiative Munich) with financial support from the Center for NanoScience (CeNS), LMUinnovativ, and the LANL LDRD program.

---

[1] F. Wang, G. Dukovic, L. E. Brus, and T. F. Heinz, Science **308**, 838 (2005).

[2] J. Maultzsch, R. Pomraenke, S. Reich, E. Chang, D. Prezzi, A. Ruini, E. Molinari, M. S. Strano, C. Thomsen, and C. Lienau, Phys. Rev. B **72**, 241402 (2005).

[3] A. Högele, C. Galland, M. Winger, and A. Imamoglu, Phys. Rev. Lett. **100**, 217401 (2008).

[4] C. Georgi, A. A. Green, M. C. Hersam, and A. Hartschuh, ACS Nano **4**, 5914 (2010).

[5] M. S. Hofmann, J. Noe, A. Kneer, J. J. Crochet, and A. Högele, Nano Lett. **16**, 2958 (2016).

[6] B. O. Tayo and S. V. Rotkin, Phys. Rev. B **86**, 125431 (2012).

[7] X. Ma, N. F. Hartmann, J. K. S. Baldwin, S. K. Doorn, and H. Htoon, Nat. Nanotechnol. **10**, 671 (2015).

[8] S. Ghosh, S. M. Bachilo, R. A. Simonette, K. M. Beckingham, and R. B. Weisman, Science **330**, 1656 (2010).

[9] X. Ma, L. Adamska, H. Yamaguchi, S. E. Yalcin, S. Tretiak, S. K. Doorn, and H. Htoon, ACS Nano **8**, 10782 (2014).

[10] X. Ma, J. K. Baldwin, N. F. Hartmann, S. K. Doorn, and H. Htoon, Adv. Funct. Mater. **25**, 6157 (2015).

[11] Y. Piao, B. Meany, L. R. Powell, N. Valley, H. Kwon, G. C. Schatz, and Y. Wang, Nat. Chem. **5**, 840 (2013).

[12] H. Kwon, A. Furmanchuk, M. Kim, B. Meany, Y. Guo, G. C. Schatz, and Y. Wang, J. Am. Chem. Soc. **131**, 6878 (2016).

[13] Y. Miyauchi, M. Iwamura, S. Mouri, T. Kawazoe, M. Ohtsu, and K. Matsuda, Nat. Photon. **7**, 715 (2013).

[14] N. F. Hartmann, S. E. Yalcin, L. Adamska, E. H. Hároz, X. Ma, S. Tretiak, H. Htoon, and S. K. Doorn, Nanoscale **7**, 20521 (2015).

[15] X. Ma, O. Roslyak, F. Wang, J. G. Duque, A. Piryatinski, S. K. Doorn, and H. Htoon, ACS

Nano **8**, 10613 (2014).

[16] X. Ma, O. Roslyak, J. G. Duque, X. Pang, S. K. Doorn, A. Piryatinski, D. H. Dunlap, and H. Htoon, Phys. Rev. Lett. **115**, 017401 (2015).

[17] N. F. Hartmann, K. A. Velizhanin, E. H. Haroz, M. Kim, X. Ma, Y. Wang, H. Htoon, and S. K. Doorn, ACS Nano **10**, 8355 (2016).

[18] X. He, N. F. Hartmann, X. Ma, Y. Kim, R. Ihly, J. L. Blackburn, W. Gao, J. Kono, Y. Yomogida, A. Hirano, et al., Nat. Photon. **11**, 577 (2017).

[19] A. Jeantet, Y. Chassagneux, C. Raynaud, P. Roussignol, J. S. Lauret, B. Besga, J. Estève, J. Reichel, and C. Voisin, Phys. Rev. Lett. **116**, 247402 (2016).

[20] T. Hümmer, J. Noe, M. S. Hofmann, T. W. Hänsch, A. Högele, and D. Hunger, Nat. Commun. **7**, 12155 (2016).

[21] R. Matsunaga, K. Matsuda, and Y. Kanemitsu, Phys. Rev. Lett. **106**, 037404 (2011).

[22] J. S. Park, Y. Hirana, S. Mouri, Y. Miyauchi, N. Nakashima, and K. Matsuda, J. Am. Chem. Soc. **134**, 14461 (2012).

[23] A. H. Brozena, J. D. Leeds, Y. Zhang, J. T. Fourkas, and Y. Wang, ACS Nano **8**, 4239 (2014).

[24] C. Möhl, A. Graf, F. J. Berger, J. Lüttgens, Y. Zakharko, V. Lumsargis, M. C. Gather, and J. Zaumseil, ACS Photonics **5**, 2074 (2018).

[25] C. Galland and A. Imamoglu, Phys. Rev. Lett. **101**, 157404 (2008).

[26] W. B. Gao, A. Imamoglu, H. Bernien, and R. Hanson, Nat. Photon. **9**, 363 (2015).

[27] J. R. Maze, P. L. Stanwix, J. S. Hodges, S. Hong, J. M. Taylor, P. Cappellaro, L. Jiang, M. V. G. Dutt, E. Togan, A. S. Zibrov, et al., Nature **455**, 644 (2008).

[28] G. Balasubramanian, I. Y. Chan, R. Kolesov, M. Al-Hmoud, J. Tisler, C. Shin, C. Kim, A. Wojcik, P. R. Hemmer, A. Krueger, et al., Nature **455**, 648 (2008).

[29] A. N. Vamivakas, Y. Zhao, S. Fält, A. Badolato, J. M. Taylor, and M. Atatüre, Phys. Rev. Lett. **107**, 166802 (2011).

[30] J. Houel, A. V. Kuhlmann, L. Greuter, F. Xue, M. Poggio, B. D. Gerardot, P. A. Dalgarno, A. Badolato, P. M. Petroff, A. Ludwig, et al., Phys. Rev. Lett. **108**, 107401 (2012).

[31] M. Hauck, F. Seilmeier, S. E. Beavan, A. Badolato, P. M. Petroff, and A. Högele, Phys. Rev. B **90**, 235306 (2014).

[32] J. C. Noe, M. Nutz, J. Reschauer, N. Morell, I. Tsioutsios, A. Reserbat-Plantey, K. Watanabe, T. Taniguchi, A. Bachtold, and A. Högele, Nano Lett. **18**, 4136 (2018).

[33] S. Mouri, Y. Miyauchi, M. Iwamura, and K. Matsuda, Phys. Rev. B **87**, 045408 (2013).

[34] S. M. Bachilo, L. Balzano, J. E. Herrera, F. Pompeo, D. E. Resasco, and R. B. Weisman, J. Am. Chem. Soc. **125**, 11186 (2003).

[35] C. Galland, A. Högele, H. E. Türeci, and A. Imamoglu, Phys. Rev. Lett. **101**, 067402 (2008).

[36] F. Vialla, Y. Chassagneux, R. Ferreira, C. Roquelet, C. Diederichs, G. Cassabois, P. Roussignol, J. S. Lauret, and C. Voisin, Phys. Rev. Lett. **113**, 057402 (2014).

[37] M. Frisch, G. Trucks, H. Schlegel, G. Scuseria, M. Robb, J. Cheeseman, G. Scalmani, V. Barone, B. Mennucci, G. Petersson, et al., Gaussian 09, Revision A. 02; Gaussian, Inc: Wallingford, CT, 2009 (2015).

[38] A. D. Becke, Phys. Rev. A **38**, 3098 (1988).

[39] M. Cossi, N. Rega, G. Scalmani, and V. Barone, J. Comput. Chem. **24**, 669 (2003).

[40] V. Barone and M. Cossi, J. Phys. Chem. A **102**, 1995 (1998).

[41] L. X. Benedict, S. G. Louie, and M. L. Cohen, Phys. Rev. B **52**, 8541 (1995).

[42] Y. Li, S. V. Rotkin, and U. Ravaioli, Nano Lett. **3**, 183 (2003).

[43] D. S. Novikov and L. S. Levitov, Phys. Rev. Lett. **96**, 036402 (2006).

[44] G. Y. Guo, K. C. Chu, D. S. Wang, and C. G. Duan, Phys. Rev. B **69**, 205416 (2004).

[45] E. N. Brothers, K. N. Kudin, G. E. Scuseria, and C. W. Bauschlicher, Phys. Rev. B **72**, 033402 (2005).

[46] B. Kozinsky and N. Marzari, Phys. Rev. Lett. **96**, 166801 (2006).

[47] K. L. Seyler, J. R. Schaibley, P. Gong, P. Rivera, A. M. Jones, S. Wu, J. Yan, D. G. Mandrus, W. Yao, and X. Xu, Nat. Nanotechnol. **10**, 407 (2015).

[48] J. Klein, J. Wierzbowski, A. Regler, J. Becker, F. Heimbach, K. Mller, M. Kaniber, and J. J. Finley, Nano Lett. **16**, 1554 (2016).

[49] D. Vella, D. Ovchinnikov, N. Martino, V. Vega-Mayoral, D. Dumcenco, Y.-C. Kung, M.-R. Antognazza, A. Kis, G. Lanzani, D. Mihailovic, et al., 2D Mater. **4**, 021005 (2017).

[50] T. G. Pedersen, Phys. Rev. B **94**, 125424 (2016).

[51] B. Scharf, T. Frank, M. Gmitra, J. Fabian, I. Žutić, and V. Perebeinos, Phys. Rev. B **94**, 245434 (2016).

[52] J. G. Roch, N. Leisgang, G. Froehlicher, P. Makk, K. Watanabe, T. Taniguchi, C. Schnenberger, and R. J. Warburton, Nano Lett. **18**, 1070 (2018).

[53] S. M. Santos, B. Yuma, S. Berciaud, J. Shaver, M. Gallart, P. Gilliot, L. Cognet, and B. Lounis,

Phys. Rev. Lett. **107**, 187401 (2011).

[54] M. Yoshida, A. Popert, and Y. K. Kato, Phys. Rev. B **93**, 041402 (2016).

[55] T. F. Ronnow, T. G. Pedersen, and H. D. Cornean, Phys. Lett. A **373**, 1478 (2009).

[56] R. J. Warburton, C. Schäflein, D. Haft, F. Bickel, A. Lorke, K. Karrai, J. M. Garcia, W. Schoenfeld, and P. M. Petroff, Nature **405**, 926 (2000).

[57] A. Gruber, A. Dräbenstedt, C. Tietz, L. Fleury, J. Wrachtrup, and C. v. Borczyskowski, Science **276**, 2012 (1997).

[58] G. Balasubramanian, P. Neumann, D. Twitchen, M. Markham, R. Kolesov, N. Mizuochi, J. Isoya, J. Achard, J. Beck, J. Tissler, et al., Nat. Mater. **8**, 383 (2009).

[59] H. J. Mamin, M. Kim, M. H. Sherwood, C. T. Rettner, K. Ohno, D. D. Awschalom, and D. Rugar, Science **339**, 557 (2013).

[60] T. Staudacher, F. Shi, S. Pezzagna, J. Meijer, J. Du, C. A. Meriles, F. Reinhard, and J. Wrachtrup, Science **339**, 561 (2013).

[61] A. Laraoui, J. S. Hodges, and C. A. Meriles, Nano Lett. **12**, 3477 (2012).

[62] Q. H. Wang, K. Kalantar-Zadeh, A. Kis, J. N. Coleman, and M. S. Strano, Nat. Nanotechnol. **7**, 699 (2012).

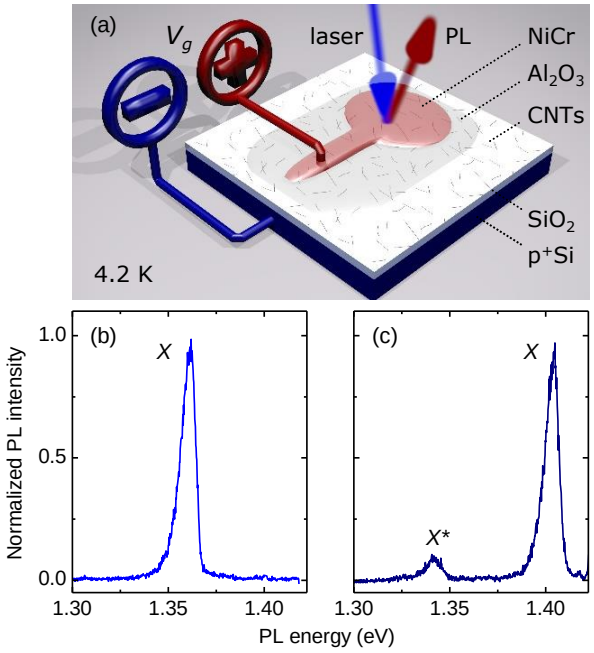

FIG. 1: (a) Schematic layout of the experiment: carbon nanotubes, dispersed in between insulating oxide layers (SiO_2 and Al_2O_3), were subjected to a transverse electric field by applying a gate voltage V_g to the semitransparent top gate (NiCr) with respect to the back gate (p-doped Si). The response of individual nanotubes to the electric field was studied with confocal excitation (laser) and detection of the photoluminescence (PL) at the temperature of liquid helium (4.2 K). (b) and (c), Photoluminescence spectra of individual nanotubes with single-peak (X) and double-peak (X, X^*) emission spectra at $V_g = 0$ V.

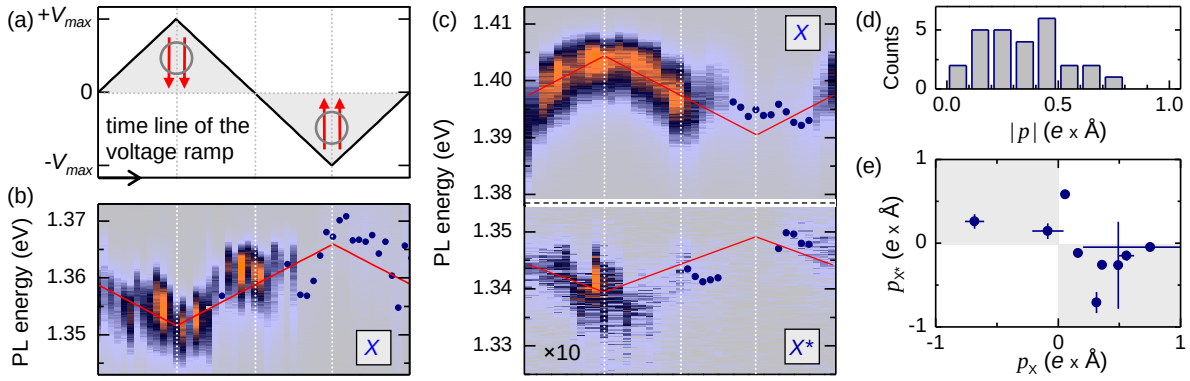

FIG. 2: (a) The transverse electric field (with orientation indicated by the inset schematics) was varied via the gate voltage from zero to $+V_{max}$, then to $-V_{max}$ and back to zero again according to the zig-zag ramp with temporal progress in sequential steps along the x-axis as indicated by the arrow. (b) and (c), False-color plots of the photoluminescence from nanotubes in Fig.1 in response to the field ramp shown in (a). In the regions of low intensity the peak maxima are shown as blue circles where peak fitting converged; the intensity in the lower panel of (c) was magnified by a factor of 10. The red solid lines are linear fits to the dispersion with slopes determined by the corresponding permanent dipole moments p. (d) Histogram of the absolute values of dipole moments extracted from linear fits as in (b) and (c) for nanotubes with emission energy in the range $1.35 - 1.43$ eV. (e) For the majority of nanotubes with double-peak emission, the signs of dipole moments of the X and X^* states, p_X and p_{X^*}, were anticorrelated (data in the grey-shaded quadrants).

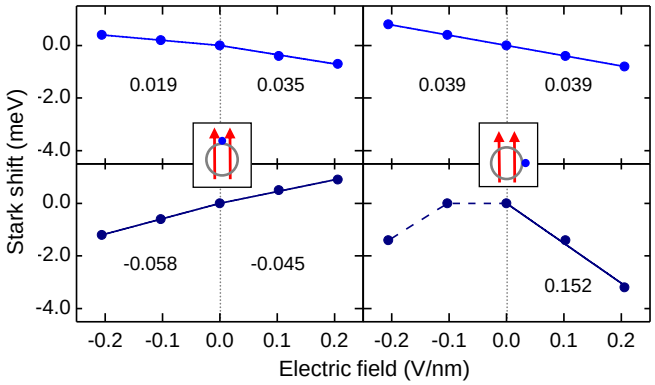

FIG. 3: Electric field dispersions of the two bright states (blue and dark blue data points in the upper and lower panels) associated with an oxygen-defect in ether-d configuration. The orientation of the defect with respect to the electric field is indicated in the inset schematics of the right and left panels. The numbers give the slopes in units of the permanent dipole moment, eÅ, extracted from linear fitting (solid lines) performed separately for positive and negative electric fields. The dashed line is a guide to the eye.

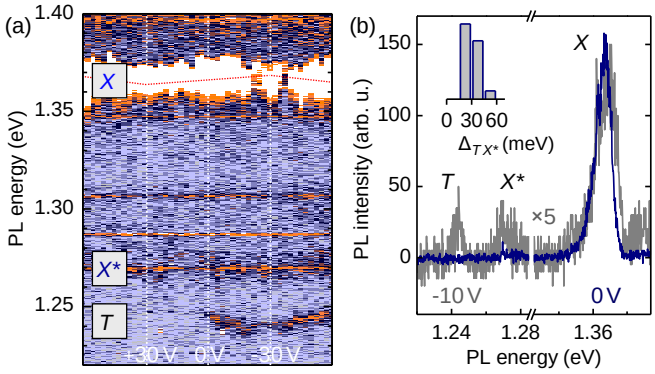

FIG. 4: (a) Logarithmic false-color plot of the photoluminescence evolution in response to a field ramp as in Fig. 2a with peak-voltage values of ±30 V. The narrow peaks are Raman sidebands of the excitation laser at 1.484 eV amplified by the logarithmic color scale. In addition to the X and X^* peaks, trion (T) satellite emission appears at negative gate voltages. (b) Photoluminescence spectra at $V_g = 0$ V (blue) and -10 V (grey, magnified by a factor of 5). The distribution of trion binding energies, as given by the energy splitting Δ_{TX^*} between the T and X^* peaks of all nanotubes with trion satellites, is shown in the inset.